Letter

Numerical simulation of vortex-induced drag of elastic swimmer models

Thomas Engels [a,b], Dmitry Kolomenskiy [c], Kai Schneider [d,*], Jörn Sesterhenn [a]

[a] ISTA, Technische Universität Berlin, Berlin, Müller-Breslau-Strasse 15, 10623 Berlin, Germany
[b] LMD-CNRS, Ecole Normale Supérieure, 24 rue Lhomond, 75231 Paris Cedex 05, France
[c] Project Team for HPC Advanced Predictions utilizing Big Data, Japan Agency for Marine-Earth Science and Technology, 3173-25 Showa-machi, Kanazawa-ku, Yokohama Kanagawa 236-0001, Japan
[d] Institut de Mathématiques de Marseille, CNRS, Aix-Marseille Université, 39 rue F. Joliot-Curie, 13453 Marseille Cedex 13, France

ARTICLE INFO

ABSTRACT

We present numerical simulations of simplified models for swimming organisms or robots, using chordwise flexible elastic plates. We focus on the tip vortices originating from three-dimensional effects due to the finite span of the plate. These effects play an important role when predicting the swimmer's cruising velocity, since they contribute significantly to the drag force. First we simulate swimmers with rectangular plates of different aspect ratios and compare the results with a recent experimental study. Then we consider plates with expanding and contracting shapes. We find the cruising velocity of the contracting swimmer to be higher than the rectangular one, which in turn is higher than the expanding one. We provide some evidence that this result is due to the tip vortices interacting differently with the swimmer.

Swimming organisms exploit bending waves to produce propulsive force, an effect which has been extensively studied. Predicting their cruising velocity, however, remains challenging, as the drag force has to be taken into account. In this work, we numerically simulate simplified "swimmers", which consist of a chordwise flexible plate with an imposed pitching motion at the leading edge, immersed in a viscous, incompressible fluid. The solid is fully coupled to the fluid, i.e., we deal with a fluid–structure interaction problem. The emphasis is placed on the longitudinal tip vortices, which result from the finite span of the plate, and their contribution to the drag force.

The usage of flexible foils for thrust generation as a simplified model for swimming organisms is common in both experimental and numerical contributions. Dewey et al. [1] for instance studied flexible pitching panels experimentally. They found the efficiency, i.e., the ratio of thrust to power coefficient, to be maximized if the Strouhal number is in the range $0.25 < St < 0.35$ and the pitching frequency is tuned to the structural resonant frequency of the foil. The former result is supported by a variety of contributions [2–4]. The connection between the driving frequency f and the resonant frequency f_0 is subject to some controversy in the community. Kang et al. [5] state that operating at or near a structural resonant will enhance performance, a fact which is widely accepted.

However, different studies found the precise relation f/f_0 to vary appreciably. For example, Ramananarivo et al. [6] state optimal performance around $f/f_0 = 0.7$. Two-dimensional data [7] points in the same direction, although the difference to the resonant is smaller. Yeh and Alexeev [8] found two regimes which maximize cruising speed and efficiency at $f/f_0 \approx 1.1$ and 1.6, respectively. However, they normalized by the resonant frequency in fluid, which can be derived analytically [9]. Contrarily to these findings, Vanella et al. [10] provided evidence for peak efficiency in flexible insect wings around 0.33. The proposed argument is the usage of superharmonic resonances, also stated in Ref. [6]. Collectively, these findings indeed suggest an important role of the resonant frequency, though the exact relation remains not fully understood.

The total drag acting on these swimming organisms or robots can be decomposed into the contributions of the friction drag and the vortex induced drag. The former contribution has been relatively well explored. Theoretical studies have considered the laminar boundary layer, which is either compressed or stretched by the undulatory motion of the swimmer [11]. This effect is usually referred to as the "Lighthill boundary-layer thinning hypothesis". More recently, Ehrenstein et al. [12] employed high-quality numerical simulations using body-fitted meshes to quantify and verify this hypothesis.

The vortex induced drag, which may play a significant role, has only recently gained attention of experimentalists. In the context of simplified mechanical swimming robots, Raspa et al. [13]

* Corresponding author.
 E-mail address: kai.schneider@univ-amu.fr (K. Schneider).

established a basic model to explain the influence of the finite aspect ratio by the formation of trailing longitudinal tip-vortices. The present numerical study is inspired by these experiments, and should be seen as complimentary approach, given the difficulty of experimentally measuring the instantaneous flow field appropriately. In a first step, using rectangular swimmers, we will reproduce some experimental results and confirm the interpretation that the tip vortices play a major role in the drag force of the swimmer. In a second step, we move on and modify the swimmer's shape and find that a contracting form may be advantageous in terms of terminal cruising speed.

The experimental swimmer used in Ref. [13] consists of a Mylar sheet attached to a driving shaft, driven by a stepper motor. The whole swimmer, including the motor, can move in the x-direction. For the numerical simulations in the present work, some assumptions are made in order to simplify the problem's complexity sufficiently.

A central assumption of our numerical swimmer is that the plate is perfectly rigid in the spanwise and flexible only in the chordwise direction. Focusing on the chordwise flexibility simplifies the complexity of the employed solid model; it is 1D. Experimental findings show that spanwise deformations are present but rather small in magnitude. Here, the swimmer is thus modeled as a slender beam, made of linearly elastic, inextensible material, undergoing large, non-linear deformations.

We parametrize the beam with its local deflection angle θ and its internal longitudinal force T. Integrating the deflection line yields, for any value of θ, automatically the same length. In other words, we can take care of the inextensibility condition by choosing this particular parametrization, since our basis function satisfies it automatically. In those variables, the governing equations read

$$\frac{\partial^2 T}{\partial s^2} - T\left(\frac{\partial \theta}{\partial s}\right)^2 = -2\eta \frac{\partial \theta}{\partial s}\frac{\partial^3 \theta}{\partial s^3} - \mu\left(\dot{\theta} + \dot{\alpha}\right)^2$$

$$-\eta\left(\frac{\partial^2 \theta}{\partial s^2}\right)^2 - [p]^{\pm}\frac{\partial \theta}{\partial s}, \tag{1}$$

$$\mu\left(\ddot{\theta} + \ddot{\alpha}\right) = -\eta\frac{\partial^4 \theta}{\partial s^4} + 2\frac{\partial T}{\partial s}\frac{\partial \theta}{\partial s} - \frac{\partial [p]^{\pm}}{\partial s}$$

$$+ \left[T + \eta\left(\frac{\partial \theta}{\partial s}\right)^2\right]\frac{\partial^2 \theta}{\partial s^2}, \tag{2}$$

together with the clamped-free boundary conditions

$$\left.\begin{array}{rcl} \theta &=& 0 \\ \frac{\partial T}{\partial s} + \eta\frac{\partial^2 \theta}{\partial s^2}\frac{\partial \theta}{\partial s} &=& 0 \\ T\frac{\partial \theta}{\partial s} - \eta\frac{\partial^3 \theta}{\partial s^3} &=& [p]^{\pm} \end{array}\right\} \text{ at clamped end,} \tag{3}$$

$$\left.\begin{array}{rcl} T &=& 0 \\ \frac{\partial \theta}{\partial s} &=& 0 \\ \frac{\partial^2 \theta}{\partial s^2} &=& 0 \end{array}\right\} \text{ at free end,} \tag{4}$$

where α is the driven pitching motion, as illustrated in Fig. 1, $[p]^{\pm}$ is the pressure jump across the beam, s is the arclength coordinate, $\mu = h\varrho_s/\ell\varrho_f$ is the dimensionless density and $\eta = EI/\ell^3\varrho_f U^2$ is the dimensionless stiffness. The material properties reported in Ref. [13] yield $\mu^{\exp} = 0.0012$ and $\eta = 0.0134$. For numerical stability reasons, we set $\mu = 0.0096$ instead, as explained later. Two-dimensional simulations confirmed that the solution is not very sensitive to the value of μ in this regime. The swimmer's length $\ell_{\text{chord}} = 0.15$ m, the fluid density $\varrho_f = 1000$ kg/m^3, a time scale $T = 1$ s and the velocity scale $U = \ell_{\text{chord}}/T$ have been
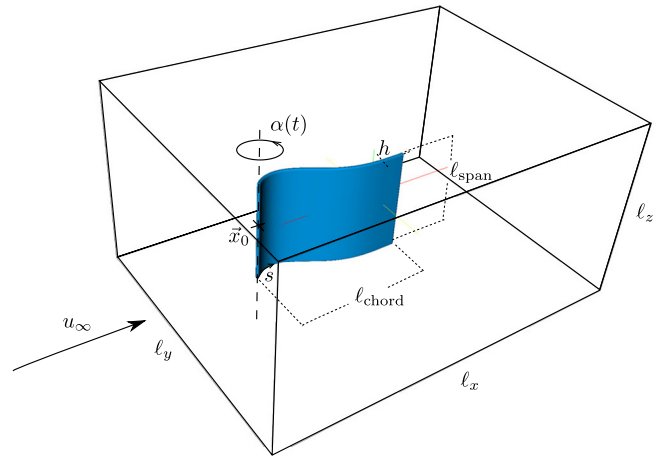

Fig. 1. Setup of the present work. The swimmer, which consists of a chordwise flexible and spanwise rigid plate undergoing an imposed pitching motion $\alpha(t)$, is immersed in a viscous incompressible fluid with imposed or dynamically computed axial mean flow u_∞.

used for normalization. Note that we assume the beam clamped in a rotating relative system, which rotates as $\alpha = \alpha_{\max}\sin(2\pi f t)$ with $\alpha_{\max} = 50°$. Therefore $\theta = 0$ at the leading edge. Contrary to the experiment, we do not vary the driving frequency f but keep it fixed at unity (thus $f = 1$ Hz). The solid model is similar to the ones used in Ref. [14,15]. The non-linear terms stem from the geometric non-linearity. The solid model equations (Eqs. (1)–(4)) are solved using finite differences with an implicit time marching scheme, which treats all terms, including the non-linear ones, implicitly. Details about the solution procedure can be found in Ref. [16,17].

The fluid is incompressible and Newtonian, and hence governed by the Navier–Stokes equations. To avoid using moving, body-fitted meshes, the flexible structure is taken into account using the volume penalization method. The governing penalized Navier–Stokes equations read

$$\partial_t \underline{u} + \underline{\omega} \times \underline{u} = -\nabla q + \frac{1}{\text{Re}}\nabla^2 \underline{u} - \frac{\chi}{C_\eta}\left(\underline{u} - \underline{u}_s\right), \tag{5}$$

$$\nabla \cdot \underline{u} = 0, \tag{6}$$

$$\underline{u}\left(\underline{x}, t = 0\right) = \underline{u}_0\left(\underline{x}\right). \tag{7}$$

Note that Eqs. (5)–(7) do not contain no-slip boundary conditions, since the geometric information is encoded in the mask function $\chi(\underline{x}, t)$ (where $\chi = 0$ in the fluid and $\chi = 1$ in the solid). In the present case, the mask thickness is set to four grid points, as problems with vanishing thickness cannot be computed using this approach. The penalization parameter C_η can be interpreted as solid permeability and is chosen to a small value, here we use $C_\eta = 10^{-3}$. Details about the penalization method for flexible obstacles can be found [16,17]. Guidelines on how to choose C_η are summarized [18]. The mask function χ and the solid velocity field $\underline{u}_s$ are constructed from the solid model.
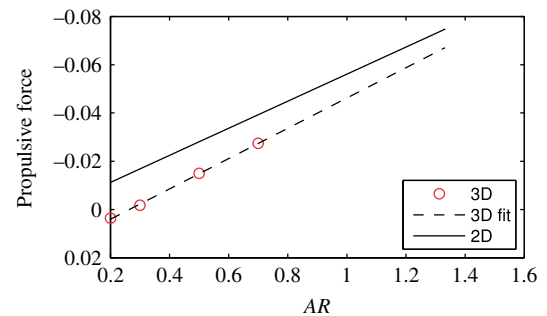
The numerical solution of Eqs. (5)–(7) is obtained in a periodic domain using a Fourier pseudospectral method and an explicit Adams–Bashforth type time stepping [19]. The grid is uniform and equidistant. Solving the Poisson equation required for the Helmholtz decomposition is done in Fourier space, where the Laplace operator is diagonal and hence the solution reduces to a simple division and no linear system has to be solved. The in-house code for producing the results is open-source and has been described [18]; it can be run on supercomputers using $\mathcal{O}(10000)$ CPUs.
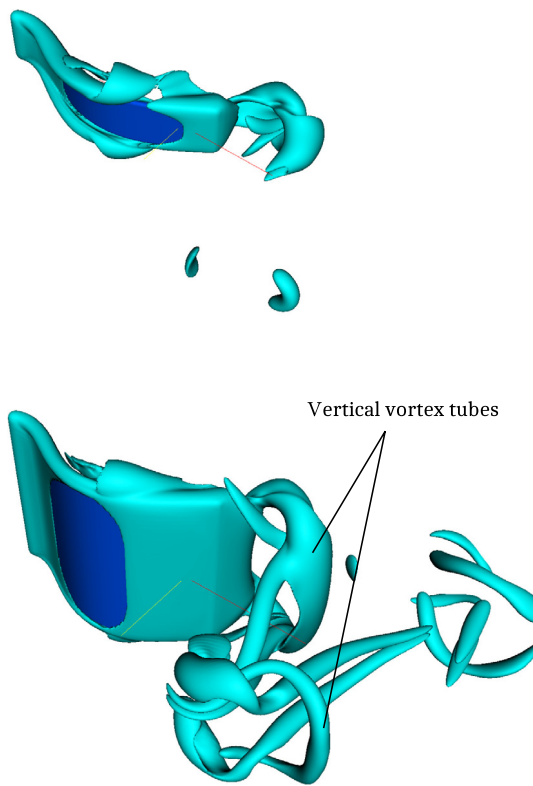
Fig. 2. Isosurfaces of vorticity $\|\underline{\omega}\| = 17.5$ for aspect ratios $AR = 0.2$ (top), $AR = 0.7$ (bottom). For $AR = 0.2$, the tip vortices dominate the flow.

Fig. 3. Thrust force as a function of the aspect ratio. The solid line represents the force predicted by the 2D approximation and the dashed line is a linear least-squares fit through the available data points from the 3D simulations.

Fluid–structure interaction problems are particularly challenging since two non-linear partial differential equations (PDEs) are coupled. The most important parameter for this coupling is the density ratio, which is defined by μ in the present article. The more similar the densities are, the more challenging the simulation. Since this work deals with swimming, performed in water, the simulations require an iterative coupling scheme. Still, as the number of iterations depends significantly on μ, we found that the experimental value $\mu^{\mathrm{exp}} = 0.0012$ requires about 15–25 iterations (each at the price of one Navier–Stokes step), while the value we used, $\mu = 0.0096$, requires only 3–5. Two-dimensional simulations confirm that the difference in results between both values is of a few per cent only, which justifies our choice of μ.

In the following we present the results obtained for rectangular plates. The Reynolds number is $Re = U\ell_{\mathrm{chord}}/\nu = 1000$, the swimmer is computed in a box of size $2.66 \times 2.00 \times 1.33$ and its leading edge at mid-span is located at $\underline{x}_0 = (0.5, \ 1.0, \ 0.66)$. At this Reynolds number, we found a resolution of $512 \times 384 \times 256$ to be sufficient. The original experiment is performed at much higher Reynolds number of $Re = 22\,500$, which is currently out of scope for numerical simulations. The value of the penalization parameter is $C_\eta = 10^{-3}$. The constant mean flow $\underline{u}_\infty = (0.5, \ 0, \ 0)$ is impulsively started at $t = 0$, and we computed a total of 5 periods. Since our discretization is periodic, a vorticity sponge term is applied to all faces of the domain to prevent vortices from re-entering the domain, with a parameter of $C_{\mathrm{sp}} = 10^{-1}$, see Ref. [17] for more information about that boundary condition. During the first period, the imposed pitching angle is multiplied by a smooth startup conditioner, in order to avoid an impulsively started motion, which would yield a pressure singularity. We carry out 4 simulations with varying aspect ratio, $AR = \ell_{\mathrm{span}}/\ell_{\mathrm{chord}} = \{0.2, \ 0.3, \ 0.5, \ 0.7\}$. In addition, a quasi-2D simulation has

been performed, in which the plate extends over the entire height of the domain. With this simulation, it was verified that the vortical structures are stable at the $Re = 1000$.

The vortical structure of the flow field is visualized in Fig. 2 for the smallest and largest values of AR, at the beginning of the fourth stroke, $t = 4.05$. In the $AR = 0.7$ case, the vertical vortex tubes can be observed. These tubes correspond to the vortices shed in the 2D case. They connect to the tip vortices and form ring-like structures, propagating perpendicular to the mean flow which also advects them downstream. It is visible that, in the $AR = 0.2$ case, the tip vortices actually dominate the wake structure—the vertical vortex tubes are not clearly distinguishable.

The thrust force, that is the x-component of the hydrodynamic force, is shown in Fig. 3. Note that the thrust points in the negative x-direction. The solid line represents the prediction based on 2D simulations. The four 3D simulations are marked by circles. It can be observed that the thrust scales almost linearly with the aspect ratio. We make the ansatz $F_x^{\mathrm{3D}} = F_{\mathrm{thrust}} \cdot AR + F_{\mathrm{tip}}$ and fit the coefficients $F_{\mathrm{thrust}} = -0.0628$ and $F_{\mathrm{tip}} = 0.0165$ using least squares to the data points. The 2D simulation returns the force per unit span, $F_{\mathrm{thrust}}^{\mathrm{2D}} = -0.0561$, and it excludes tip-vortices by definition. We can therefore estimate the thrust as $F_x^{\mathrm{2D}} = F_{\mathrm{thrust}}^{\mathrm{2D}} \cdot AR$, which is equivalent to a finite sized swimmer without tip-vortices.

We can thus observe that the values for the thrust per unit span are quite similar in both 3D and 2D cases, $F_{\mathrm{thrust}} \approx F_{\mathrm{thrust}}^{\mathrm{2D}}$, and that the tip vortices indeed act like a constant offset. We can thus numerically confirm the experimental results of Raspa et al. [13].

The results for rectangular plates illustrate the importance of tip vortices for the total drag. Actual fish on the other hand have of course non-rectangular caudal fins, with possible consequences for the vortical structures in the wake. We choose an additional set of two different shapes, an expanding and a contracting form, to study their influence on the cruising speed. All shapes have the same surface and follow the same imposed driving motion. For simplicity, we still assume the mechanical structure to be 1D and with constant μ and η, although the varying $\ell_{\mathrm{span}}(s)$ suggests that both should depend on s. This is a first order approximation, since both μ, η are linear in ℓ_{span}, but as $\eta \propto h^3$ the dominant effect of the stiffness η is captured and as μ is small anyways (light swimmer), this assumption seems justified. The non-rectangular shapes are defined as $\ell_{\mathrm{span}}^{\mathrm{exp}}(s) = 2\left(\frac{0.35}{2} + 0.525 s^2\right)$, $\ell_{\mathrm{span}}^{\mathrm{contr}}(s) = 2\left(\frac{1.05}{2} - 0.525 s^2\right)$ and are illustrated in Fig. 4.

Our swimmers remain anchored to the laboratory system and move the surrounding fluid instead. The mean flow in the axial direction is thus computed dynamically from $\dot{u}_\infty = \langle F \rangle / m_{\mathrm{fluid}}$, where the initial condition is $u_\infty(t = 0) = 0$. In the steady state, the mean flow balances the thrust force $\langle F \rangle$. The fluid mass is set to a relatively small value, $m_{\mathrm{fluid}} = 0.1235$, in order to speed-up the computation. Note that the cruising speed is not perfectly
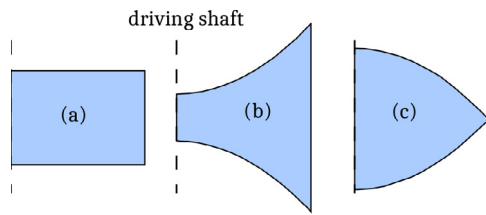
Fig. 4. Different shapes investigated here, termed (a) "rectangular", (b) "expanding" and (c) "contracting". All three shapes have the same surface.
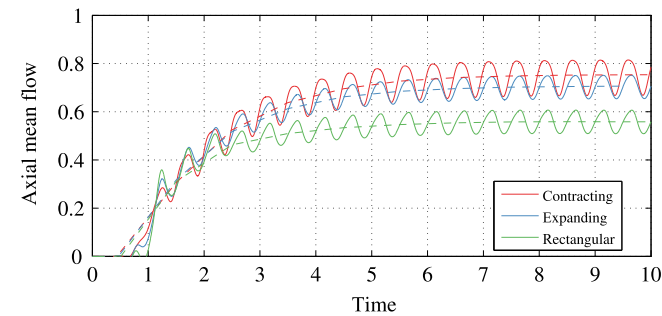

Fig. 5. Axial mean flow over time for the three different swimmers from Fig. 4. Solid lines represent instantaneous data, and dashed lines represent a moving average over the duration of one stroke.

Fig. 6. Isosurfaces of vorticity $\|\underline{\omega}\| = 17.5$ for contracting (top) and expanding shapes (bottom).

constant in the steady state, hence the Galilean invariance is only satisfied approximately. Fig. 5 illustrates the result obtained for all swimmers. They all reach their steady state within 10 strokes, but the resulting cruising speed significantly depends on the swimmer's shape. The contracting shape ($u_\infty = 0.75$) outruns both the rectangular ($u_\infty = 0.70$) and the expanding ($u_\infty = 0.55$) shapes.

One remarkable difference between the three simulations is that the expanding one has the smallest trailing edge displacement, which is due to the larger concentration of area there. The pressure acting on the tail is thus much higher in that case, reducing the deflection amplitude.

All swimmers have finite span and thus exhibit tip vortices, and again these vortices offer a potential explanation for the higher cruising velocity of the contracting shape. A priori, one might think the expanding form is advantageous, since the larger trailing edge will produce larger vertical tube vortices (cf Fig. 2), and thus reduce the spurious three-dimensional effects.

However, the opposite is true. Fig. 6 shows the vortical structures for the contracting and expanding shape at the same time, which is during the steady cruising state. The tip vortices, shed in both configurations around mid-chord, are advected downstream due to the mean flow, and they can be associated with a zone of lower pressure. This drop in pressure creates a local net force pointing in the direction of the vortex core, and part of which contributes to the total drag force (depending on the orientation of the surface normal relative to the x-direction). Visibly, in the contracting case, the tip vortex quickly loses contact with the actual swimmer—its tip-vortex induced drag is thereby reduced. The opposite is true for the expanding type swimmer: not only does the tip vortex not lose contact with the swimmer, it does instead even increase the portion of the swimmer influenced by the tip vortices, compared to the rectangular swimmer. It can also be noted that the total mean enstrophy, $\langle Z \rangle = \left\langle \iiint \|\underline{\omega}\|^2 \, d\underline{x} \right\rangle$, which is a measure for the dissipation in the fluid wake, is significantly higher in the expanding than in the contracting case, $\langle Z \rangle_{\text{contracting}} =$
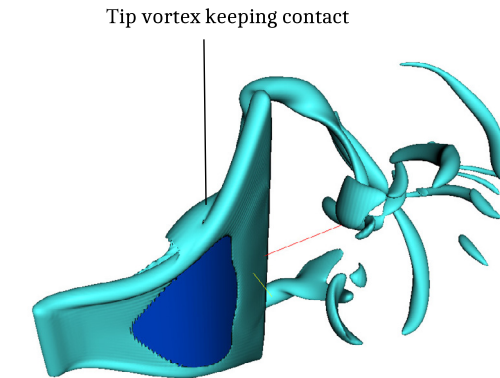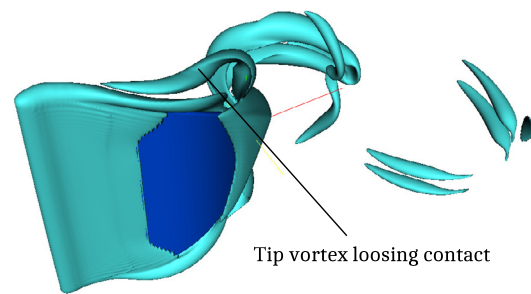
98.7 versus $\langle Z \rangle_{\text{expanding}} = 127.7$, indicating a higher dissipation rate in the expanding case.

We numerically simulated the flow past simplified elastic swimmer models. These models consist of flexible plates that have a driven pitching angle at their leading edges. In the first part, we simulated rectangular swimmers, that are inspired by the experimental work presented in Ref. [13]. We support the finding that the tip vortices, or, more generally, 3D effects, significantly contribute to the total drag, and thus should be taken into account when predicting the cruising speed of these swimmers. We illustrated that indeed the 3D nature of these flows may act like an tip-vortex induced drag that is virtually independent of the aspect ratio. In a second step we investigated the shapes other than rectangular, namely a contracting and an expanding one, and compared their cruising velocities. We found that the contracting shape is the best, and postulate that this may possibly be explained by the tip vortices quickly "losing touch" to the swimmer, which reduces their influence on the drag. Caudal fins resembling the expanding shape are found in many fish (thunniform fin), while the contracting form is found in some amphibians (protocercal form).
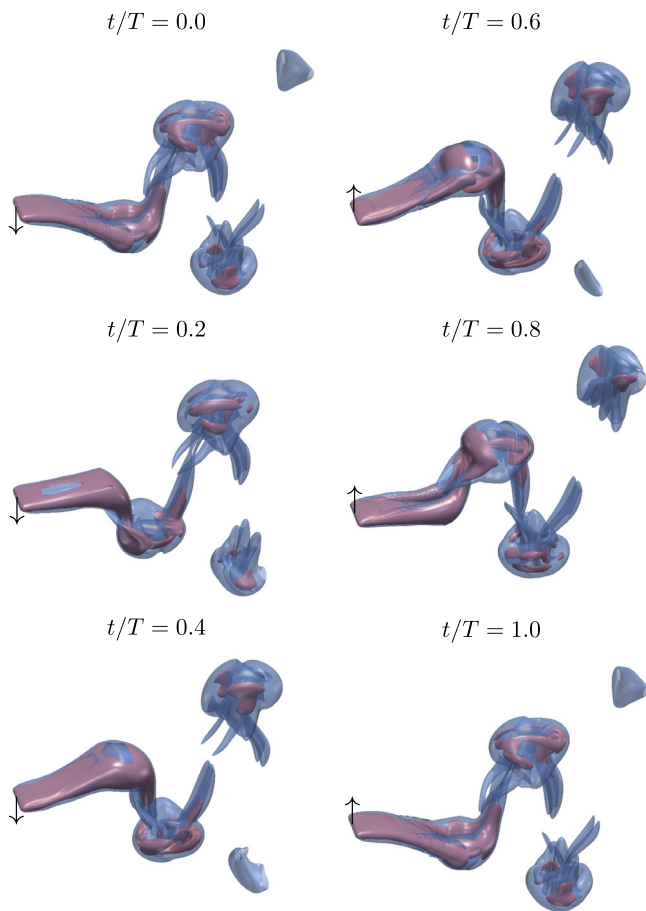
Appendix

As validation case we consider the numerical work presented in Ref. [8]. That study considers a flexible panel with an imposed

Table A.1
Cycle-averaged results for the heaving plate.

	u_∞	P_{aero}	η_{eff}	d
Yeh and Alexeev [8]	1.47	5.11	0.29	7.60
Present	1.40	6.53	0.22	7.68

Fig. A.1. Flow generated by the heaving plate, visualized by isosurfaces of vorticity magnitude. Blue semi-transparent corresponds to $\|\underline{\omega}\| = 5$, and purple corresponds to $\|\underline{\omega}\| = 20$. The Reynolds number is 250.

heaving motion at the leading edge with zero angle of attack (i.e., no pitching imposed). The authors study the influence of the driving frequency, normalized by the eigenfrequency in fluid, $\phi = f/f_{1,f}$ by varying the elastic properties of the flexible plate. Two regimes are identified, which maximize either the velocity for $\phi \approx 1.1$ or the efficiency for $\phi \approx 1.7$. The reference solution is computed using the Lattice–Boltzmann method, which approximates incompressible fluid flow without solving an elliptical Poisson equation. An overset approach with a refined region in the vicinity of the plate and a coarser one in the far field are used. The flexible plate is modeled using the lattice-spring model, i.e., it is approximated as a system of mass points connected by springs.

Here, we consider only a single simulation out of the dataset presented in Ref. [8], arbitrarily fixing the added mass parameter (as defined in Ref. [8]) to $T = 1$ and the frequency ratio to $\phi = 1.1$. The non-dimensional solid properties in our model are $\mu = 0.4031$ and $\eta = 1.6669$. The plate's width is $w = 0.4$, and the prescribed heaving motion is given as $y = a_0 \cos(2\pi f t)$, where $a_0 = 0.1$. The Reynolds number is $Re = 2\pi f \ell a_0 / \nu = 250$. The domain

size is $4 \times 4 \times 2$ and it is discretized using $768 \times 768 \times 384$ points, with the penalization parameter equal to $C_\eta = 2 \times 10^{-4}$. We apply a vorticity sponge to remove the periodicity. The validation is performed in the steady cruising state. The handling of the mean flow is the same as above, using $m_{fluid} = 0.5$. In coarser resolution pre-runs, the mean flow was started from rest and the terminal value reached in that simulation, 1.3, was set as initial condition $u_\infty(t = 0)$ in the high-resolution case, to further reduce the computational cost. In the high-resolution case, 11 cycles were performed.

Table A.1 compares the results obtained during the last cycle with those given in [8]. The cruising speed is slightly reduced in the present work, but the agreement to within 5% is still tolerable. The aerodynamic power, which can be computed as $P_{aero} = \int \underline{u}_s (\underline{u} - \underline{u}_s) / C_\eta dV$ when using the penalization method [18], is overpredicted by about 25%. Both, overprediction of power requirement and underprediction of cruising speed are related to an elevated drag coefficient owing to the smoothing layer in the χ-function. The trailing edge displacement d is very close to the reference solution (1%).

The flow field is visualized in Fig. A.1. At each half-stroke, a vortex is shed, which travels perpendicular to the mean flow on a V-shaped path. The flow field is qualitatively similar to the reference computation.

In conclusion, the comparison yields reasonable agreement with the literature, and the remaining difference can be attributed to differences in modeling. The present plate is rigid in the lateral direction, while the reference data are obtained with a 2D flexible plate. This simplification has also an influence on the solid model parameters η and μ. The former is the non-dimensional rigidity, corrected by the Poisson ratio of the solid material [20]. Owing to this correction, the eigenfrequency in vacuum of the beam, $f_0 = 3.516/2\pi \sqrt{\eta/\mu}$ is slightly different (6%) from the corresponding eigenfrequency of the 2D flexible plate. However, the differences between both studies are reasonable and we thus conclude that our fluid–structure interaction module is validated.

References

[1] P.A. Dewey, B.M. Boschitsch, K.W. Moored, et al., Scaling laws for the thrust production of flexible pitching panels, J. Fluid Mech. 732 (2013) 29–46.
[2] C. Eloy, Optimal Strouhal number for swimming animals, J. Fluids Struct. 30 (2012) 205–218.
[3] M. Triantafyllou, A. Techet, F.S. Hover, Review of experimental work in biomimetic foils, IEEE J. Ocean. Eng. 29 (2004) 585–594.
[4] G.S. Triantafyllou, M.S. Triantafyllou, M.A. Grosenbaugh, Optimal thrust development in oscillating foils with application to fish propulsion, J. Fluid Struct. 7 (1993) 205–224.
[5] C.-K. Kang, H. Aono, C.E.S. Cesnik, et al., Effects of flexibility on the aerodynamic performance of flapping wings, J. Fluid Mech. 689 (2011) 32–74.
[6] S. Ramananarivo, R. Godoy-Diana, B. Thiria, Rather than resonance, flapping wing flyers may play on aerodynamics to improve performance, Proc. Natl. Acad. Sci. USA 108 (2011) 5964–5969.
[7] D. Kolomenskiy, T. Engels, K. Schneider, Numerical modelling of flexible heaving foils, J. Aero Aqua Bio-Mech. 3 (2013) 22–28.
[8] P.D. Yeh, A. Alexeev, Free swimming of an elastic plate plunging at low Reynolds number, Phys. Fluids 26 (2014) 053604.
[9] C.A.V. Eysden, J.E. Sader, Frequency response of cantilever beams immersed in viscous fluids with applications to the atomic force microscope: Arbitrary mode order, J. Appl. Phys. 101 (2007) 044908.
[10] M. Vanella, T. Fitzgerald, S. Preidikman, et al., Influence of flexibility on the aerodynamic performance of a hovering wing, J. Exp. Biol. 121 (2009) 95–105.
[11] M.J. Lighthill, Large-amplitude elongated-body theory of fish locomotion, Proc. R. Soc. Lond. B 179 (1971) 125–138.
[12] U. Ehrenstein, M. Marquillie, C. Eloy, Skin friction on a flapping plate in uniform flow, Phil. Trans. R. Soc. A 372 (2014) 20130345.
[13] V. Raspa, S. Ramananarivo, B. Thiria, et al., Vortex-induced drag and the role of aspect ratio in undulatory swimmers, Phys. Fluids 26 (2014) 041701.
[14] S. Alben, Simulating the dynamics of flexible bodies and vortex sheets, J. Comput. Phys. 228 (2009) 2587–2603.

[15] S. Michelin, S.L. Smith, B. Glover, Vortex shedding model of a flapping flag, J. Fluid Mech. 617 (2008) 1–10.

[16] T. Engels, D. Kolomenskiy, K. Schneider, et al., Two-dimensional simulation of the fluttering instability using a pseudospectral method with volume penalization, Comput. Struct. 122 (2012) 101–112.

[17] T. Engels, D. Kolomenskiy, K. Schneider, et al., Numerical simulation of fluid-structure interaction with the volume penalization method, J. Comput. Phys. 281 (2015) 96–115.

[18] T. Engels, D. Kolomenskiy, K. Schneider, et al., FluSI: A novel parallel simulation tool for flapping insect flight using a Fourier method with volume penalization, SIAM J. Sci. Comput. 38 (2016) S3–S24.

[19] K. Schneider, Numerical simulation of the transient flow behaviour in chemical reactors using a penalisation method, Comput. & Fluids 34 (2005) 1223–1238.

[20] L. Landau, E. Lifshitz, Theory of Elasticity, third ed., in: Theoretical Physics, vol. 7, Butterworth-Heinemann, 1986.